





RESEARCH ARTICLE

10.1029/2021JD036373

The Climate and Ozone Impacts of Black Carbon Emissions From Global Rocket Launches

Christopher M Maloney^{1,2} , Robert W Portmann² , Martin N Ross³ , and Karen H Rosenlof² ¹Cooperative Institute for Research in Environmental Sciences, Boulder, CO, USA, ²National Oceanic and Atmospheric Administration, Boulder, CO, USA, ³The Aerospace Corporation, El Segundo, CA, USA

Key Points:

- The increased stratospheric BC burden from rocket launches warms the stratosphere
- Stratospheric BC-induced heating causes shifts in stratospheric dynamics, year-round NH ozone loss, and a stronger Antarctic ozone hole
- The climate response scales in a near linear fashion with increasing rocket launch emissions

Supporting Information:

Supporting Information may be found in the online version of this article.

Correspondence to:

C. M. Maloney,
christopher.maloney@noaa.gov

Citation:

Maloney, C. M., Portmann, R. W., Ross, M. N., & Rosenlof, K. H. (2022). The climate and ozone impacts of black carbon emissions from global rocket launches. *Journal of Geophysical Research: Atmospheres*, 127, e2021JD036373. <https://doi.org/10.1029/2021JD036373>

Received 20 DEC 2021

Accepted 18 MAY 2022

Abstract Aerosol emissions from spaceflight activities play a small but increasing role in the background stratospheric aerosol population. Rockets used by the global launch industry emit black carbon (BC) particles directly into the stratosphere where they accumulate, absorb solar radiation, and warm the surrounding air. We model the chemical and dynamical response of the atmosphere to northern mid-latitude rocket BC emissions. We initially examine emissions at a rate of 10 Gg per year, which is an order of magnitude larger than current emissions, but consistent with extrapolations of space traffic growth several decades into the future. We also perform runs at 30 and 100 Gg per year in order to better delineate the atmosphere's response to rocket BC emissions. We show that a 10 Gg/yr rocket BC emission increases stratospheric temperatures by as much as 1.5 K in the stratosphere. Changes in global circulation also occur. For example, the annual subtropical jet wind speeds slow down by as much as 5 m/s, while a 10%–20% weakening of the overturning circulation occurs in the northern hemisphere during multiple seasons. Warming temperatures lead to an ozone reduction in the northern hemisphere by as much as 16 DU in some months. The climate response increases in a near linear fashion when looking at larger 30 and 100 Gg emission scenarios. Comparing the amplitude of the atmospheric response using different emission rates provides insight into stratospheric adjustment and feedback mechanisms. Our results show that the stratosphere is sensitive to relatively modest BC injections.

Plain Language Summary Emissions from spaceflight activities play an increasing role in the background stratospheric aerosol population. Rockets used by the global launch industry emit black carbon particles directly into the stratosphere where they accumulate, absorb solar radiation, and warm the surrounding air. We model the climate response of the stratosphere to an annual, black carbon emission source from rocket launches. We initially examine an emission rate of 10 Gg per year, an order of magnitude larger than current emissions but plausible within the next two decades based upon recent trends in space traffic growth. We also perform runs at 30 and 100 Gg per year in order to better understand the atmosphere's response to rocket black carbon emissions. We show that the rocket black carbon increases stratospheric temperatures and changes the global circulation, both of which cause a reduction in the total ozone column, mainly in the northern high latitudes. Comparing the amplitude of the atmospheric response using different emission rates provides insight into stratospheric adjustment and feedback mechanisms. Our results show that the stratosphere is sensitive to relatively modest black carbon injections.

1. Introduction

Aerospace combustion emissions have long been recognized as a potentially important source of gases and particles for the atmosphere (Penner et al., 1999). Most of the past research has focused on emissions from jet engine powered subsonic aircraft that fly mainly in the troposphere. The climate and ozone impact from gaseous subsonic aircraft emissions are well understood. CO₂ and H₂O emissions act to warm the surface. The particles produced by subsonic jet aircraft are far more complex and less well understood. Particles associated with jet engines include black carbon (BC), sulfate aerosol, and contrail ice clouds. The impact of these particles covers a broad range of direct and indirect radiative and chemical processes.

Modeling studies have examined a hypothetical fleet of supersonic and hypersonic aircraft (i.e., Grewe et al., 2007; Kinnison et al., 2020; Matthes et al., 2022; Zhang et al., 2021a; Zhang et al., 2021b). These aircraft emit jet exhaust directly into the stratosphere during cruise producing an atmospheric response quite different from that of subsonic aircraft (i.e., Lee et al., 2010). Due in part to a higher emission altitude, the aerosols emitted by supersonic aircraft have a larger impact on ozone chemistry and a much longer stratospheric lifetime than

those from subsonic aircraft. Though such emissions currently do not occur, there is value in modeling theoretical aircraft because the modeled components and altitudes can be isolated and varied and the stratospheric processes involved can be better understood.

Rocket engines present a real and growing source of stratospheric combustion emissions. Launch rates have more than tripled in the past decade (Ailor, 2021; Jones, 2018) and the expectation is for accelerated growth in the coming decades (Jones, 2018). Rockets play a unique role in the middle atmosphere as they represent the only source of human-produced aerosol emissions. Due to the use of a number of different propellant combinations and engine technologies, rocket engine combustion differs fundamentally from jet combustion. All rocket engines emit CO₂, CO, H₂O, and H₂ in varying combinations depending on engine type and altitude. Gaseous emissions from hydrogen fueled rockets are thought to not present a significant source of global change (Larson et al., 2017). Aerosol emissions, and in particular absorbing aerosol such as BC, have greater potential for environmental impacts.

Rocket emissions are unique in that there are many propellant combinations and engine types, each with a specific particulate emission character. One propellant type (H₂ fuel) emits no particles but rather H₂O and could be considered “clean” (Larson et al., 2017). However, most rocket engines burn a hydrocarbon in some form, usually in a fuel-rich combustion chamber, and so emit BC particles. The BC emission index EI(BC) during flight in the stratosphere is thought to be as large as 30–50 g/kg (De Luca et al., 2013; Simmons, 2001; Strykowski, 2001 and see Supporting Information S1), two orders of magnitude larger than the EI(BC) for jet engines at high altitude cruise (Stettler et al., 2013). A heavy launcher (10³ tons of propellant) using kerosene fueled high EI(BC) engines emits on the order of 10 tons of BC into the stratosphere during each launch. While the global launch fleet burns less than 0.1% of the fuel that global aviation burns in the stratosphere, the factor of 100 larger EI(BC) suggests that the current stratospheric BC burden from rockets is comparable to the BC burden from present day aircraft that fly in the stratosphere (Ross & Toohey, 2019). Solid rocket motor engines (SRMs), in addition to BC emission, release alumina particulate emissions as large as 300 g/kg; their coupled impacts have yet to be examined. Recently developed hydrocarbon fuels (including methane) are likely to produce BC similar to kerosene fuel; however, direct measurements have not been made. The focus of this study is on the widely used kerosene burning rocket engines.

Most rocket emission studies have focused on the impacts of gas and aerosol emissions from chlorinated solid rocket motors (SRMs). Nevertheless, the potential for rocket BC emissions to impact stratospheric chemical and dynamical processes has long been recognized (Blake & Kato, 1995; Newman et al., 2001; Ross & Toohey, 2019; Turco et al., 1980). In situ plume measurements of ozone loss in a mixed propellant plume (Ross et al., 2000) implicated BC from a kerosene engine as a cause of ozone loss. Ross et al. (2010) used a coarse model of the global atmosphere (sans ozone chemistry) to predict the climate impact of 0.6 Gg of rocket emissions. They showed negative radiative forcing of about 50 mW/m² with a 2.4 Gg accumulation of BC in the stratosphere. BC can potentially interact with stratospheric ozone in multiple ways: (a) BC absorbs solar radiation and emits heat. Increased temperatures influence the loss rate of ozone destroying reactions (World Meteorological Organization (WMO), 2018); (b) BC may acquire layers of sulfate coating as it ages which will increase sulfate surface area density (SulfSAD). A larger SulfSAD means more surfaces for heterogeneous chemistry to occur; (c) Shifts in stratospheric dynamics due to changing temperature can further alter stratospheric ozone concentrations (WMO, 2018).

Direct stratospheric BC emissions from the growing space industry fall into a poorly studied stratosphere regime with BC injection rates much smaller than nuclear conflict scenarios, yet larger than present day global aviation BC emissions (Lee et al., 2021). Insofar as the first order atmospheric response to stratospheric BC emissions is not sensitive to the precise nature of the source, our work has application to understanding the atmosphere's dynamical and chemical response to stratospheric BC injections in general.

The primary goal of this work is to extend the earlier study by Ross et al. (2010) suggesting that BC emitted by rocket engines is a potentially important stratospheric pollutant. We perform simulations using BC emissions from a hypothetical rocket source representing an unspecified combination of BC emitting rocket types in order to evaluate how an expanded space travel industry could affect climate and ozone. In order to bracket the range of emission strengths and to better understand the subtle features of the model's behavior, a range of BC source strengths are investigated including 10, 30, and 100 Gg per year, emitted into the northern midlatitude

stratosphere. The lower value is about a factor of 10 greater than present day rocket BC emissions and could, extrapolating recent growth, represent actual emissions within two decades (see Supporting Information S1). The primary purpose of this study is to evaluate the climate response from a plausible 10 Gg/yr emission scenario. The 30 and 100 Gg/yr emission scenarios are purely hypothetical at this time. The larger emission scenarios are used to provide context for investigating how the climate response may scale with greater emissions. For a frame of reference, recent wildfire pyroCb events such as the Australian event in December 2019 injected approximately 20 Gg BC into the stratosphere, while the August 2017 Pacific Northwest event injected 5–6 Gg of BC (Yu et al., 2019, 2021).

2. Methods

In this study, we use the Whole Atmosphere Community Climate Model version 6 model (WACCM6; Gettelman et al., 2019; Marsh et al., 2013) within the state-of-the-art Community Earth Systems Model version 2 (CESM2, Danabasoglu et al., 2020). The model was run at a 2° longitude \times 2° latitude resolution instead of the default Gettelman et al. (2019) $1^\circ \times 1^\circ$ resolution. WACCM6 has 70 vertical levels extending from the surface to 6×10^{-6} hPa (140 km). The Modal Aerosol Model version 4 (MAM4) was chosen to represent aerosol processes for this study (Liu et al., 2016). This differs from the Community Aerosol and Radiation Model for Atmospheres (CARMA; Mills et al., 2008; Toon et al., 1988) used in Ross et al. (2010). The primary difference between MAM4 and CARMA is the representations of aerosol size distributions. MAM4 is a modal model which possess four size modes (Aitkens, accumulation, coarse, and a primary carbon mode). Modes are assumed to be log-normal with a fixed width, but varying in radius. Within each mode, MAM4 tracks two values for each aerosol species: (a) the mass of the aerosol species, and (b) the total number concentration of aerosols within the mode. Number density is assumed to be internally mixed among aerosols within a given mode while aerosol mass is treated as externally mixed among aerosol within the mode. CARMA is a sectional model that represents mass and number with a binned size distribution. This means that within each CARMA size bin, the mass and number for aerosols are individually represented and tracked. The number of size bins within the CARMA aerosol model is a tunable parameter. While CARMA has a more detailed representation of aerosol size distribution, MAM4 has been shown to confidently represent atmospheric black carbon (Liu et al., 2016) with a considerably lower operational cost than CARMA making MAM4 ideal for long-term simulations.

MAM4 treats two types of black carbon (BC), a freshly emitted pure black carbon and an aged black carbon aerosol with a sulfate coating. Fresh black carbon acquires sulfate layers and is transferred to the aged BC mode within MAM4 (Liu et al., 2016). The BC aging process is sensitive to the mass concentrations of both the BC core and the coating materials with aging of fresh BC occurring on the scale of hours to days within MAM4 (Liu et al., 2016; Wang et al., 2018). Aged BC is added into the stratospheric sulfate surface density calculation and therefore influences heterogeneous chemistry within CESM2/WACCM6.

A control case using default BC surface and aircraft emissions in CESM2 is used to evaluate the BC perturbed runs. We implemented a 10 Gg per year rocket BC emission scenario, which is a factor of 20 times larger than the annual emissions used in Ross et al. (2010) and about a factor of 10 greater than current rocket BC emissions. An analogous natural phenomenon to a 10 Gg/yr emission is the recent historic 2019/2020 Australian bushfire pyroCb event which emitted 0.9 Tg of smoke containing approximately 22 Gg of BC into the lower stratosphere (Yu et al., 2021). However, the spatial and temporal BC emission pattern differs considerably between a wildfire and rocket launch. While a large wildfire will inject all of its emissions into the lower stratosphere, a rocket launch releases BC over the entire vertical extent of the stratosphere (see Supporting Information S1). Furthermore, the wildfire release is a limited injection while rockets are a nearly constant source. Though different, comparative analysis of the climate response between the two scenarios, as components of the stratospheric background, are instructive.

The 10 Gg/yr emission corresponds to a linear extrapolation of recent space travel growth for two decades. The actual recent launch trend and projected launches based on regulatory approvals indicates accelerated growth (Murtaza et al., 2020). Unlike aviation, space travel does not have a sufficient historical basis on which to make firm projections and we acknowledge the speculative nature of our scenario. Two larger emission scenarios of 30 Gg per year and 100 Gg per year were also investigated in order to (a) understand the impacts of an extremely large future space travel emissions scenario and (b) more clearly elucidate the adjustments and feedbacks that

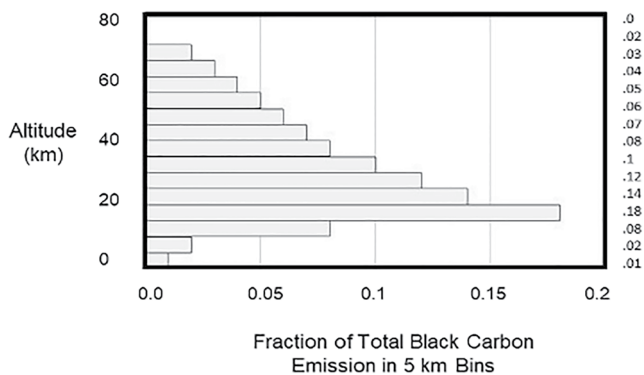


Figure 1. Fraction of BC emission in each 5 km altitude bin as a function of altitude for a typical orbital rocket launch first stage using hydrocarbon fuel (left). For each model level within a 5 km bin, the emissions are uniformly distributed. The vertical distribution follows from assuming constant propellant flow, typical trajectory, and secondary combustion (afterburning) that consumes BC emitted during tropospheric flight. The amount of BC emitted at the rocket engine nozzle exit plane is constant with time and altitude; the amount that remains in the cold plume varies with altitude. The afterburning process consumes 100% of BC at 0 km and 0% at 15 km altitude. For a typical launch trajectory about 50% of the total propellant is burned in the troposphere only 3% of the total BC emission is there. Second stage emissions are typically much smaller than first stage emissions (<10%) and are often of the H_2/O_2 propellant type that does emit BC; second stage is not included here.

determine the atmosphere's response. These are discussed at the end of this paper.

The rocket BC is emitted at a constant rate throughout the year. BC emissions were placed in a single horizontal grid box located at approximately 30 N, 80 W which corresponds to an emissions weighted average of the various launch sites on Earth. We note that while the launch pattern used in this study is based on present day space traffic, the future global launch pattern could look different with rockets launched at different latitudes. A change in the latitude of the launch pattern would likely impact the climate response, but such a scenario was not investigated in this study. The BC emission is deposited vertically between 5 and 70 km according to a typical launch trajectory (see Text S1 in Supporting Information S1 and Figure 1). BC emissions are uniformly released across each model level within each 5 km altitude bin. Note that while approximately 50% of the total first stage hydrocarbon propellant is burned in troposphere, secondary combustion in the trailing plume reduces BC emissions to negligible concentrations below 15 km (see Text S1 in Supporting Information S1 and Figure 1). Thus, the mass emissions simulated here are sourced from the cold plume.

Each scenario was simulated using both a fixed sea surface temperature (SST) configuration and an interactive ocean configuration. Using two types of ocean configurations differs from Ross et al. (2010) who only performed fixed SST simulations. The fixed SST configuration uses repeating year 2000 SST while the interactive ocean is initialized with year 2000 conditions. The merit of using a fixed SST data ocean is that it permits one to isolate the stratospheric response to the BC emissions while reducing internal variability and allowing for the effective radiative forcing to be more clearly estimated. In

the interactive ocean configuration, the simulated ocean is allowed to evolve with the changing climate. An evolving ocean is useful for capturing the full temperature and dynamical responses to the BC emissions. The atmosphere in each scenario was also initialized with year 2000 conditions. This means fixed background emissions for aerosols, greenhouse gases, chlorofluorocarbon (CFC), and other radiatively important features. While year 2000 conditions were used for this study, other initialization years could be used, each of which would impact how ozone responds to the perturbations presented here. Each simulation was run for a total of 50 years, ending in 2050. We excluded the first 10 years to ensure the ocean/climate has reached steady state in the fixed SST case, as well as to allow for the stratospheric BC concentration to reach steady state (red shading, Figure S1 in Supporting Information S1). Note that WACCM does not produce a consistent internal quasi-biannual oscillation (QBO) without additional parameterization. The QBO is known to impact ozone and circulation in the NH. We recognize that the lack of a consistent QBO will influence the climate response shown here.

3. Results

3.1. Stratospheric Black Carbon Loading

Emissions of 10 Gg/yr results in a quasi-steady state 40 Gg annual stratospheric BC burden after 6 years (black line, Figure S1 in Supporting Information S1); four times larger than the assumed annual emission and consistent with the estimated stratospheric overturning time equal to 4–5 years (i.e., Butchart, 2014; Li et al., 2012; Linz et al., 2017; Waugh and Hall, 2002). The increased stratospheric BC burden in the 10 Gg/yr emission scenario creates a stratospheric “umbrella” (Ross & Vedda, 2018) that can be seen at nearly all latitudes (Figure 2). The control background stratospheric BC burden is about 11 Gg (Table 1) so the speculative rocket scenario equals a 230% increase in stratospheric BC burden.

The colored contours in Figure 2 show the aged BC concentration while the contour lines represent fresh BC concentration. The control case shows the influence of naturally occurring surface and aviation BC emissions with limited incursion of BC in the stratosphere. The largest BC burden increase occurs in aged BC between 12 and 40 km and covers mid and polar latitudes of the northern hemisphere (20–90 N). In a thick layer between

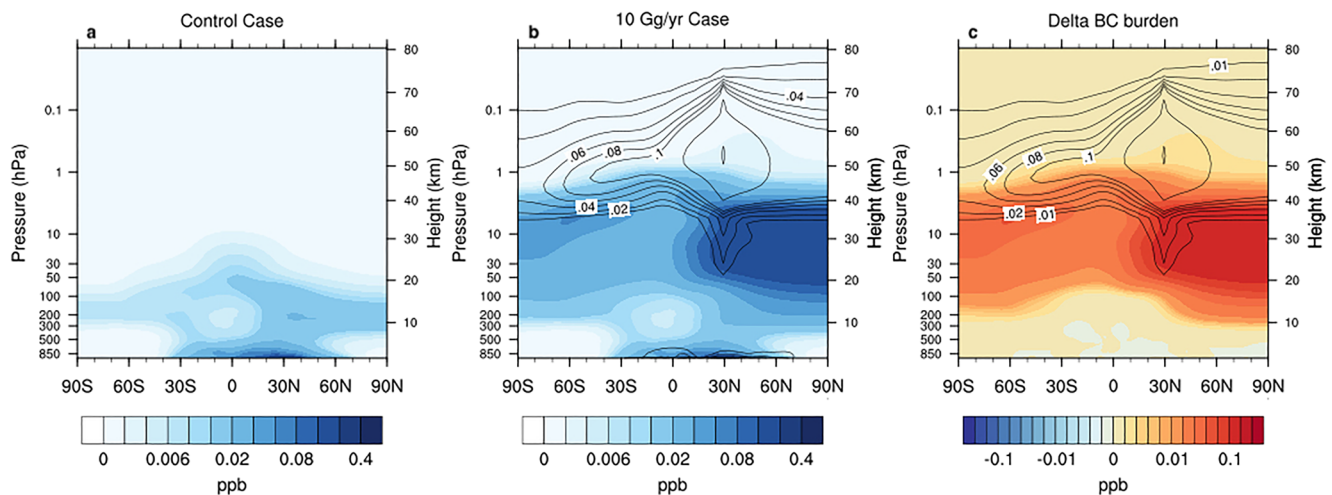


Figure 2. Annual zonal average of black carbon mixing ratio over the final 40 years of the simulation. Panel (a) shows the control case BC mixing ratio while panel (b) shows the 10 Gg emission case. Panel (c) shows the change in BC mixing ratio due to the addition of a 10 Gg/yr emission (10 Gg/yr case—control case). The colored contours represent aged BC, while the contour lines represent the fresh BC burden only in the stratosphere on the same scale. The units for both the colored and line contours are parts-per-billion. Tropospheric fresh BC is not plotted, and there is no fresh BC emitted in the stratosphere for the control case, so no contour lines are shown in Panel (a).

19 and 40 km in the NH, the BC zonal burden increases by as much as 0.4 ppb (Figure 1c), exceeding the base aviation related BC mixing ratio peak near 12 km at 40 N (Figure 2a).

A second maximum comprised of fresh BC (approximately 0.2 ppb) occurs at higher altitudes (40–70 km) between 10 and 60 N. The fresh BC persists at much higher altitudes compared to aged BC because there is less sulfate available in the upper stratosphere to be deposited onto the surfaces of aging BC aerosols. As long as fresh BC remains in the upper stratosphere, it will age slowly; however, as fresh BC sediments into the mid-to-lower stratosphere where sulfate is more abundant, fresh BC will acquire a sulfate coating and become aged BC. As a result, aged BC will have a larger maximum than fresh BC because a fraction of fresh BC has fallen out of the upper stratosphere and been converted into aged BC below 40 km. This dependence on sulfate concentration and the rate of fresh BC sedimentation into the mid-to-lower stratosphere leads to the BC distribution exhibited by

Table 1
Annually Averaged Climate Anomalies for Each Emission Scenario

	Control simulation	10 Gg case	30 Gg case	100 Gg case
Average stratospheric BC burden (Gg)	11	39	100	340
Stratospheric T (K)	250 ± 0.040	0.16 ± 0.051	0.51 ± 0.058	1.5 ± 0.050
Surface T (K)	280 ± 0.053	−0.0071 ± −0.85	−0.083 ± −0.081	−0.19 ± −0.079
O ₃ (DU)	280 ± 0.79	−3.5 ± −1.3	−9.05 ± −1.0	−20 ± −1.2
TOA all-sky net flux (W/m ²)	−29 ± −0.083	0.076 ± 0.11	0.15 ± 0.11	0.47 ± 0.11
200 mb all-sky SW flux (W/m ²)	180 ± 0.078	−0.14 ± −0.11	−0.39 ± −0.10	−1.1 ± −0.11
200 mb all-sky LW flux (W/m ²)	200 ± 0.049	0.16 ± 0.062	0.37 ± 0.067	1.2 ± 0.074
TOA clear-sky net flux (W/m ²)	−6.0 ± −0.071	0.0022 ± 0.11	−0.056 ± −0.098	−0.13 ± −0.10
200 mb clear-sky SW flux (W/m ²)	220 ± 0.069	−0.21 ± −0.076	−0.57 ± −0.088	−1.7 ± −0.090
200 mb clear-sky LW flux (W/m ²)	220 ± 0.050	0.18 ± 0.070	0.43 ± 0.070	1.4 ± 0.075

Note. The left column displays the annual average and year-to-year variability in each listed simulation field from the control case. The uppermost row shows the annual mean stratospheric BC burden in gigagrams. The three right columns contain the annual average anomaly (Emission simulation—Control Simulation) for the 10 Gg (middle-left), 30 Gg (middle-right), and 100 Gg (far right) emission cases for each of the listed simulation fields. The annual variability in the delta values is provided. Statistically significant anomalies are represented by bold text. Note that the mean values and anomalies for radiative fluxes, column ozone, and stratospheric temperature come from the fixed SST simulation while the surface temperature values come from the interactive ocean simulation. That bold text was there to indicate statistical significance.

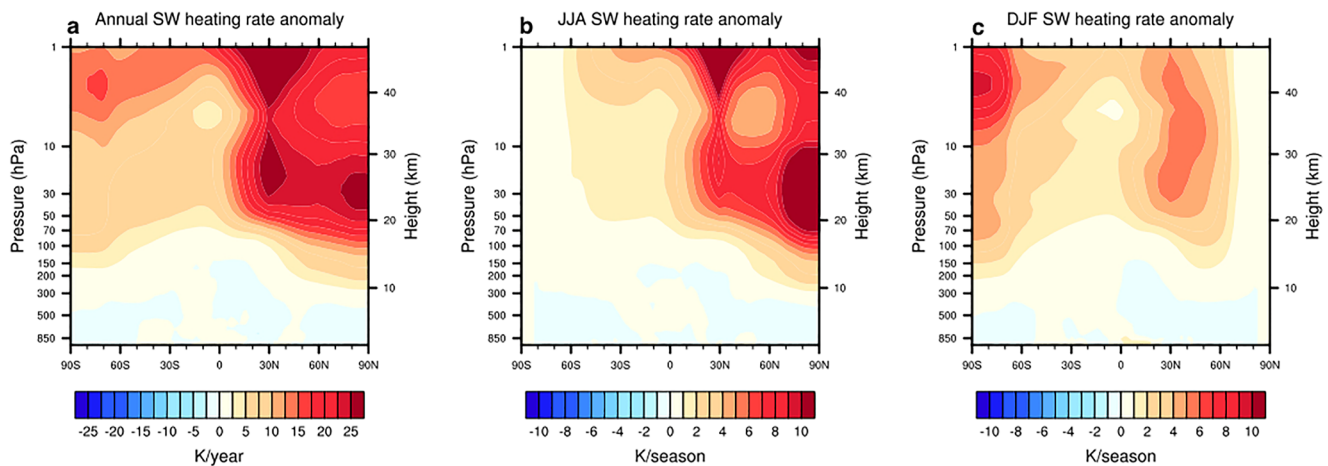


Figure 3. Clear-sky shortwave heating rate anomaly for the final 20 years of the fixed SST ocean simulations (10 Gg/yr case—default) calculated using the WACCM double call option to remove aerosol heating. The annual average is shown in panel (a), while the JJA and DJF seasons are shown in panels (b) and (c), respectively.

Figure 2. Considering aged BC and fresh BC together, the NH vertical spatial pattern of the 10 Gg/yr BC burden in Figure 2 is consistent with the emission profile shown by Figure 1.

The southern hemisphere (SH, 20°–90°S) experiences a more modest increase in aged BC that reaches a maximum of 0.08 ppb between 30 and 40 km at 60°S (Figure 2b). Fresh BC also can be found in the SH at higher altitudes, but at lower concentrations. This is a nearly 100% increase in BC mixing ratio in the SH stratosphere. Figure 2 shows that the stratospheric emissions in the NH are transported across all latitudes in the stratosphere, though the transport is not efficient.

The more extreme, 30 and 100 Gg/yr emission scenarios produce a spatially similar stratospheric BC distribution to the 10 Gg/yr case, except that the stratospheric BC burden is larger. More BC can also be seen making its way into the upper troposphere and lower stratosphere (UT/LS) below 200 mb in both hemispheres as well (Figures S2 and S3 in Supporting Information S1).

3.2. Temperature Response to BC Emissions

Earlier studies have shown that an increase in stratospheric BC concentration will warm the stratosphere (i.e., Kravitz et al., 2012; Larson et al., 2017; Mills et al., 2008; Ross et al., 2010; Ross & Vedula, 2018). BC absorption of incoming shortwave radiation produces a rise in temperature and an increase in longwave emission. The amount of warming depends on the relative sizes of the dynamical and radiative timescales that strongly vary with altitude and latitude. Figure 3 shows the change in the clear-sky shortwave heating rate due to the 10 Gg/yr emission under a fixed SST ocean scenario. All anomalies discussed in the remainder of this manuscript are the rocket emission scenario minus the control simulation (i.e., 10 Gg/yr—Control).

The spatial pattern of the annual shortwave heating rate anomaly is proportional to the stratospheric BC concentration; the largest warming is in the NH coincident with the largest increase in BC concentration (Figures 2b and Figure 3a). The seasonal response shows that the summertime stratosphere experiences a strong positive shortwave heating rate anomaly (Figures 3b and 3c). However, the DJF season still experiences a modest increase in shortwave heating in the NH as a result of the significant amount of stratospheric BC absorbing sunlight throughout the year, as well as changes in the global circulation, discussed below.

Figure 3 shows a pervasive negative shortwave heating rate anomaly near the surface with a maximum slightly south of the BC emission latitude (30°N). This surface anomaly in the fixed SST simulation is in agreement with earlier findings from Ross et al. (2010) who predicted an approximately 0.25 K cooling to occur beneath the injection latitude. These results demonstrate the similarity in the atmospheric response among anthropogenic perturbations of stratospheric aerosols (e.g., Weisenstein et al., 2015). In more general terms, increased stratospheric aerosols cause hemisphere-wide negative shortwave anomalies at the surface.

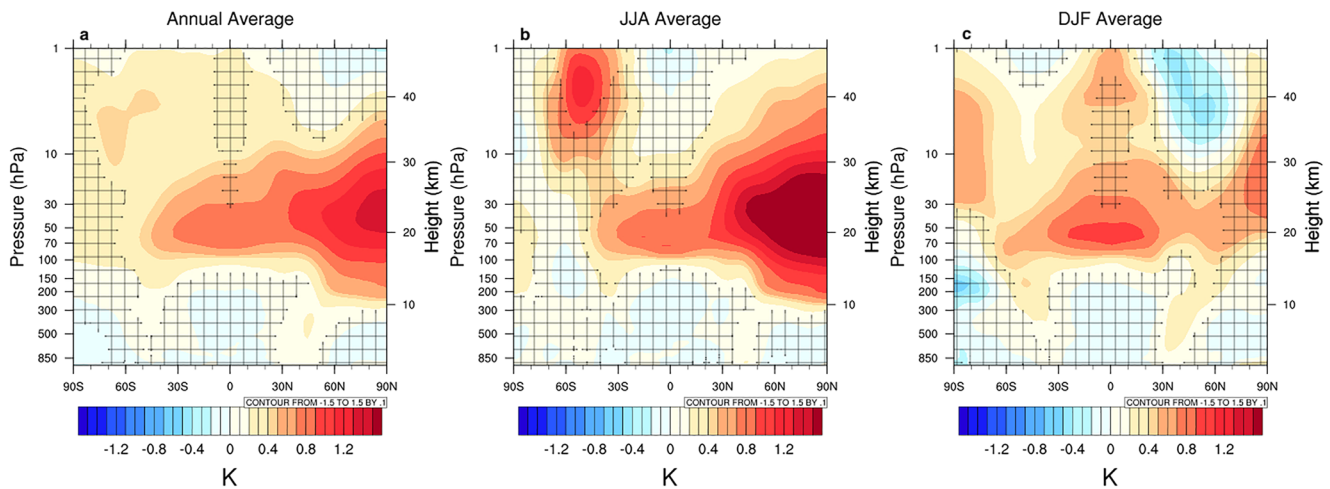


Figure 4. The annual average zonal temperature anomaly (10 Gg/yr—Control) for the interactive ocean simulation is shown in panel (a), the JJA season average anomaly is shown in panel (b), and the DJF season average anomaly is shown in panel (c). Statistically significant anomalies occur in areas where no shading can be seen in the panel (95% confidence interval).

Figure 4 depicts the atmospheric temperature response to a 10 Gg/yr emission in an interactive ocean simulation. The annual zonal average temperature anomaly shows statistically significant (95th percentile, non-hatched areas) warming in most of the stratosphere with the amount of warming proportional to the BC concentration (Figure 4a). In the tropics, a 0.6 K warming occurs at 20 km (possibly related to ozone changes) increasing to 1.5 K at the north pole. Furthermore, the vertical extent of the statistically significant heating expands to a range of 10–35 km nearer to the north pole (Figure 4a).

Though the annual SH BC burden is smaller than in the NH, statistically significant annual heating still occurs in this hemisphere. A 0.3 K warming anomaly occurs equatorward of 60°S and covers nearly the entire vertical extent of the SH stratosphere (Figure 4a). A slightly stronger warming of 0.5 K occurs between 30 and 40 km at 60°S where the greatest increase in SH BC was shown in Figure 2. We note that this annual SH burden, approximately 12 Gg, is on a similar scale as the 2019 Australian bushfire SH BC injection. The 30 and 100 Gg cases show similar yet larger stratospheric warming responses (Figures S4 and S5 in Supporting Information S1).

At the Earth's surface and in contrast to Figure 3 and Ross et al. (2010), which suggests a hemisphere-wide cooling associated with absorption and reflection of solar SW by the stratospheric particles, a statistically significant annual heating (approximately 0.25 K) occurs in a narrow band between 30° and 50°N (Figure 4a). This warming is interesting because it is located directly underneath the maximum in the rocket BC burden. This surface warming primarily occurs during the DJF season but also has a weak signal in the JJA season (Figures 4b and 4c). Though less prominent in the annual average, the DJF season also experiences an equally strong tropospheric warming between 30° and 50°S that doesn't reach to the surface like the NH surface warming.

Neither hemisphere experiences a surface warming in our fixed SST simulation (not shown) meaning this feature is unique to the interactive ocean simulation. Furthermore, the larger emission scenarios of 30 and 100 Gg/yr do not see the same tropospheric warming anomaly. Instead, larger emissions result in a troposphere with pockets of statistically significant cooling (Figures S4 and S5 in Supporting Information S1) and a cooling anomaly of 0.08–0.2 K in the global average surface temperature (Table 1). It is possible that a dynamical shift unique to the 10 Gg/yr emission scenario could lead to the tropospheric warming signal in Figure 4, but the dynamical response in this region of the atmosphere is too noisy to discern any clear features from Figure 5. More significant BC loading below 200 mb in the UT/LS NH beneath the larger emission scenarios could also contribute the differences in the tropospheric temperature response between the 10 Gg/yr simulation and the larger emission scenarios (Figures S2 and S3 in Supporting Information S1). Lastly, there is a possibility that so much BC in the UT/LS artificially changes properties of other MAM4 aerosols due to MAM4 shortcomings (Visoni et al., 2022), resulting in the discrepancy shown here. We cannot clearly define the cause of the tropospheric warming signal in Figure 4, but it is unlikely that this signal is robust (Table 1). Further modeling is required to understand this unexpected feature of the 10 Gg/yr case.

Wind Anomalies

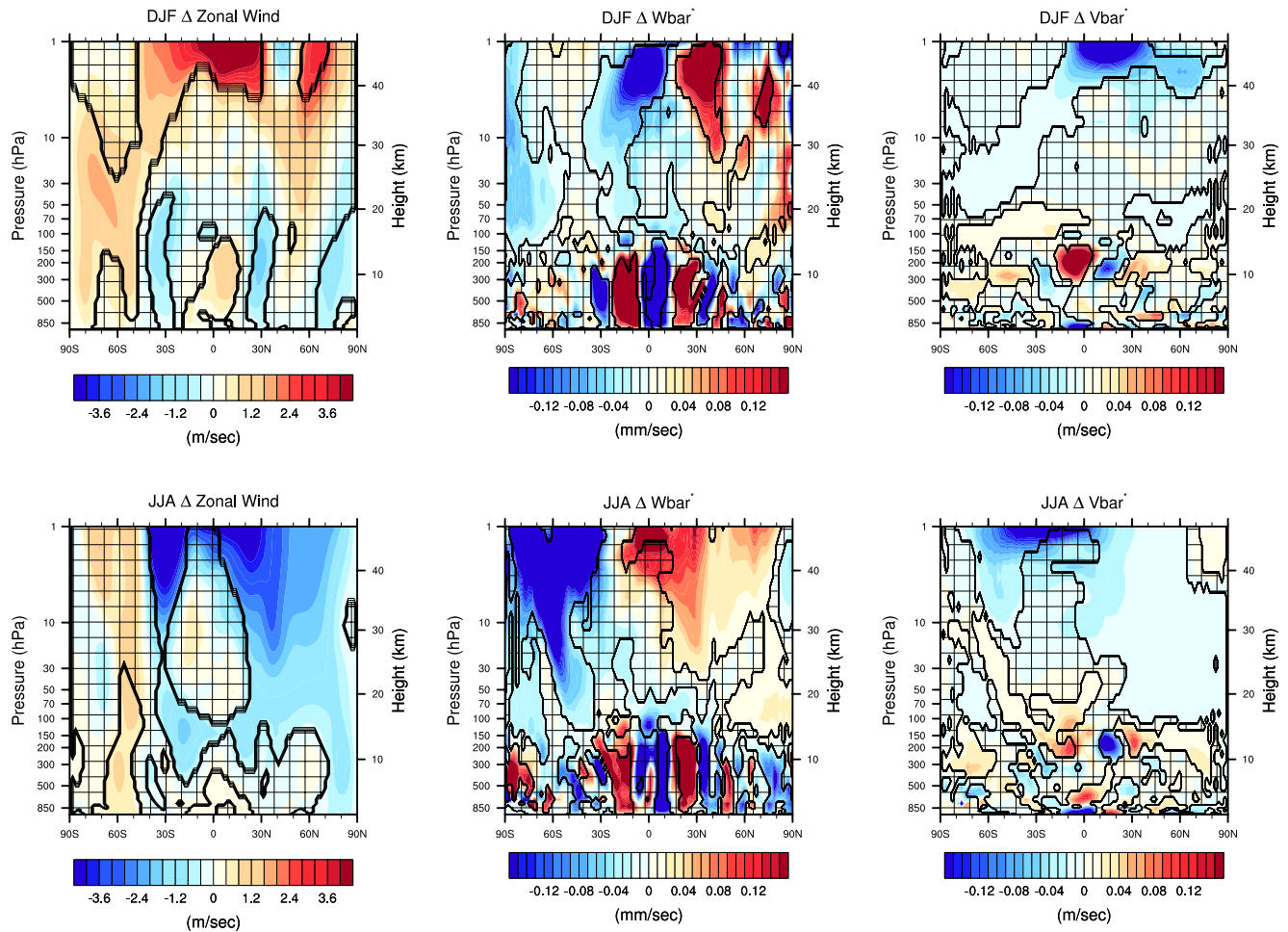


Figure 5. Seasonal wind anomaly residual for the DJF (top row) and JJA seasons (bottom row) for the interactive ocean simulation. Zonal wind is shown in panels (a) and (d), \bar{w}^* residuals are shown in panels (b) and (e), and meridional wind residuals are shown in panels (c) and (f). Areas where no shading exist are statistically significant against annual variability (95% confidence interval). Anomalies can be interpreted for each graph as follows: a positive zonal wind anomaly means stronger westerly flow, a positive \bar{w}^* anomaly means stronger uplift, and a positive meridional wind anomaly means stronger northward flow.

It is evident from Figure 4 that the stratospheric annual warming anomaly is dominated by the JJA season (Figure 4b). The NH JJA experiences as much as a 2 K warming poleward of 50 N, four times as strong as the DJF anomaly in the same region. Furthermore, the annual 40 km warming at 60°S is clearly seen in the SH JJA winter-time season. The DJF stratospheric temperature anomaly (Figure 4c) possesses a similar, but weaker warming pattern to that of the JJA season in the extra-tropics; however, the DJF season warming signal is stronger and is vertically more extensive than the JJA season in the tropics. Both seasonal warming responses compare relatively well with the seasonal shortwave heating from Figure 3, but there are differences. These differences are likely due to the fact that while increased shortwave heating can cause significant warming, stratospheric temperatures are also sensitive to changes in stratospheric dynamics and radiative processes associated with changes in ozone.

In contrast to the hemispherical responses, a year-round warming of 0.8 K occurs at 20 km in the tropics and is primarily caused by warming during the DJF season (Figures 4a and 4c). Figure 6b and 6c shows that ozone increases by as much as 0.3 DU/km at 20 km in the 0°–30°S latitude band and may be the source of this tropical warming. A likely cause for this lower altitude ozone layer is that statistically significant ozone loss occurs directly above between 30 and 50 km because of the BC caused warming (Figure 6c). With less ozone above and where the solar elevation remains high during all seasons, self-healing can occur as more UV light penetrates deeper into the stratosphere and invigorate the Chapman Cycle at lower altitudes.

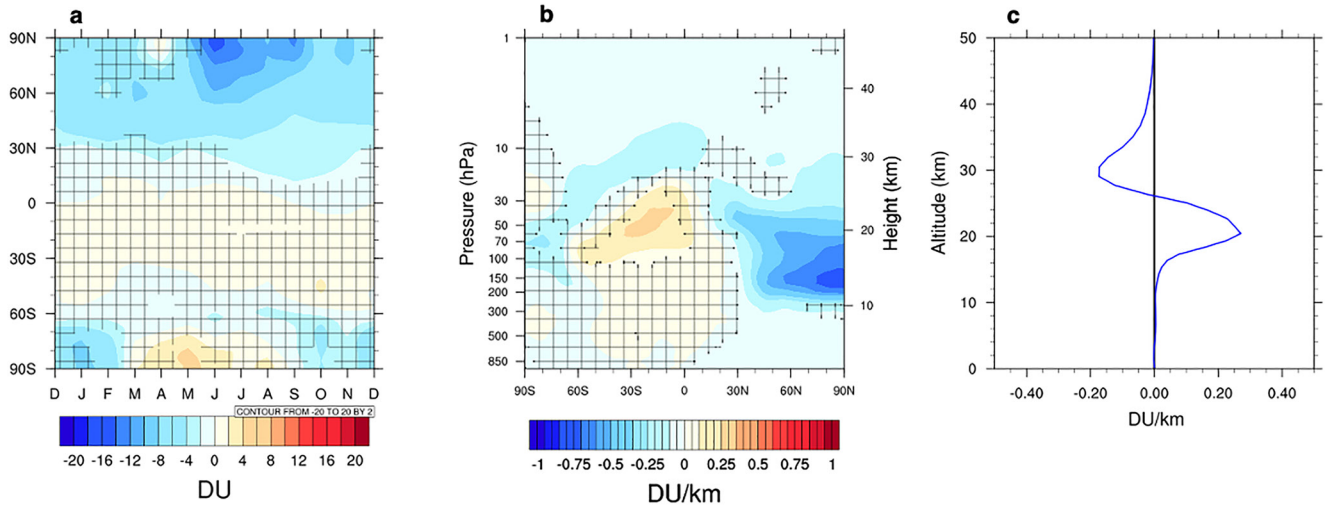


Figure 6. The total column ozone anomaly (DU) is shown in panel (a). Column ozone anomaly has been converted into monthly averages and plot against latitude. The annual zonal average ozone anomaly is shown in DU/km in panel (b). Statistically significant ozone anomalies are in areas where with no hatched lines (95% confidence interval). Panel (c) shows the vertical profile of the annual ozone anomaly in DU/km from the surface to 50 km between 5° and 30°S. The interactive ocean simulation was used to produce this figure.

Overall, our larger 10 Gg/yr emission scenario experiences a stronger warming response than what was shown in Ross et al. (2010). This is consistent with the factor of 20 larger emission rate assumed here. Furthermore, the spatial distribution of the temperature anomaly deviates from the DJF zonal temperature profile shown in figure 3 of Ross et al. (2010). Where they find only pockets of statistically significant warming, we see statistically significant warming over most of the stratosphere that is twice as strong in some locations like the tropics. Likewise, our simulations show NH and SH warming in a midlatitude band where Ross et al. (2010) found a cooling signal. The higher fidelity of WACCM6 illustrates how subtle regional changes such as shifts in circulation patterns and shortwave heating rate combine to produce a small net global signature at the surface.

3.3. Stratospheric Dynamical Response to BC Emissions

One of the primary responses to the BC induced stratospheric warming is a change in atmospheric dynamics. Figure 5 shows the seasonal zonal wind anomaly residuals for the DJF (top row) and JJA (bottom row) seasons in the interactive ocean simulation. Near the stratopause, the mid-latitude DJF NH westerlies accelerate by approximately 3.5 m/s at 60°N, while the tropical easterlies slow down by as much as 5 m/s (Figure 5a). Lower in the NH stratosphere, both the NH subtropical and polar jets slow down. In the SH, the summertime upper stratospheric easterlies weaken by 2 m/s. Like with the NH, the SH subtropical jet weakens, but at a less significant rate. Conversely, the SH polar jet increases. An analysis of simulated streamlines (not shown) revealed that the zonal wind anomalies are due to a change in wind speed magnitude instead of a shift in latitude position.

Anomalies in the DJF residual circulation (Figures 5b and 5c) show that a shift in the global overturning circulation occurs. Noise in the model troposphere makes it difficult to discern the exact impact that the 10 Gg/yr emission has upon the vertical and meridional winds; however, from Figures 5b and 5c it can be seen that the tropical ascending and poleward flowing branches of the Hadley cell slow in both hemispheres. At higher altitudes, tropical ascending flow decreases by as much as 0.2 mm/s, and the poleward flowing deep branch of the overturning circulation near the stratopause weakens (Figures 5b and 5c). These vertical and meridional wind anomalies fall between 10% and 20% of the magnitude of normal wind speeds.

The JJA zonal wind anomaly shows a different response from the DJF season (Figure 5d). In the JJA NH, upper stratospheric summertime easterlies strengthen by as much as 5 m/s while the SH upper stratospheric wintertime westerlies weaken by more than 5 m/s. In the SH lower stratosphere and troposphere, wintertime zonal winds strengthen below the polar jet at 60°S by approximately 1.5 m/s. Elsewhere in the lower stratosphere and troposphere the zonal wind anomalies signify weaker winds (Figure 5d).

The JJA tropospheric vertical and meridional wind response is similar to that for DJF; however, the stratospheric response is different (Figures 5e and 5f). The deep branch of the overturning circulation, which is now flowing toward the south pole during the JJA season, strengthens. Statistically significant uplift occurs in the stratospheric NH tropics while the downwelling polar branch in the SH increases by over 10%. Furthermore, poleward meridional flow in the wintertime hemisphere strengthens by 20%.

When considering the annual and seasonal temperature anomalies shown in Figure 4, the stratospheric dynamical responses appear consistent with seasonal variability and the larger thermal anomaly in the NH where the BC source is located. The global overturning circulation controls the overall flux of air from the warm tropics to the cold poles. During JJA, a large stratospheric warm pool forms in the NH which extends from the lower stratosphere tropics to the entire vertical extent of the stratosphere near the pole (Figure 4b). A warmer NH strengthens the meridional temperature gradient which in turn strengthens the transport of air to the wintertime south pole.

The DJF stratospheric flow weakens for similar reasons. Both the SH and NH stratosphere experience statistically significant warming during DJF (Figure 4c). Because of this, the NH wintertime meridional temperature gradient is weaker than the control case, thus the poleward transport of mass weakens.

Both of the larger 30 Gg/yr (Figure S6 in Supporting Information S1) and 100 Gg/yr (Figure S7 in Supporting Information S1) emission scenarios produce different DJF seasonal wind anomalies compared to the 10 Gg/yr case. Like with the 10 Gg/yr case, the NH mid-latitude stratospheric westerlies strengthen in windspeed, but the latitude of the positive wind anomaly shifts farther northward as the amount of BC emitted per year increases (Figures S6 and S7 in Supporting Information S1). Eventually, the positive zonal wind anomaly is confined poleward of 60° N under the 100 Gg/yr case (Figure S7a in Supporting Information S1). Tropical uplift continues to weaken further under the larger emission scenarios while an increase in uplift occurs between 30° and 60° N. As was previously mentioned, under the 10 Gg/yr emission scenario, both upper stratospheric meridional transport and descent at the NH pole slow down. Under the larger emission scenarios however, the sign of both anomalies becomes positive, indicating faster transport of air north of 60° N. The SH stratosphere winds in the DJF season slow in response to the 30 and 100 Gg/yr emissions. The polar jet winds reduce by as much as 2 m/s in the 100 Gg/yr case (Figure S7a in Supporting Information S1). Descent at the poles also slows by as much as 1.5 mm/s. While the DJF winds changed when perturbed with a more significant annual BC emission, the JJA response in the 30 and 100 Gg/yr emission scenarios remain relatively similar to the 10 Gg/yr case. Figures S6 and S7 in Supporting Information S1 show that BC emissions under the larger emissions scenarios would have drastic impacts on stratospheric winds and transport.

3.4. Black Carbon and Ozone Loss

Temperature, dynamics, and ozone all strongly influence one another (i.e., WMO, 2018). Therefore, it is unsurprising that the 10 Gg/yr emission scenario, which we have shown above to induce significant changes in stratospheric temperatures and winds also cause changes in stratospheric ozone. The following discussion of the stratospheric ozone response is based on results produced by the interactive ocean simulation. Statistically significant ozone depletion occurs poleward of 30° N in nearly all months of the year (Figure 6a). Within this latitude band the most significant ozone destruction (approximately 16 DU or about 4%) occurs in June at the north pole. All other locations north of 30° N experience at least a 4 DU ozone loss throughout the year. Most of the NH ozone is lost between 10 and 20 km where a greater than 0.5 DU/km ozone anomaly can be seen poleward of 30° N (Figure 6b). Additional statistically significant ozone loss exceeding 0.1 DU/km occurs at most altitudes in the NH. The spatial pattern of the negative NH ozone anomaly directly coincides with the zonal BC distribution and positive warming anomaly shown previously.

The SH ozone response remains within annual model variability except during the DJF season where a -8 DU anomaly occurs at the south pole. A statistically significant ozone reduction of 6 DU also occurs at the south pole during the month of October, which is of particular interest as the Antarctic ozone hole forms at this time. Therefore, Figure 6 suggests that the Antarctic ozone hole may become more severe as a result of stratospheric rocket emissions. Also of note is a statistically significant increase in ozone (2 DU) during the month of May (Figure 6a).

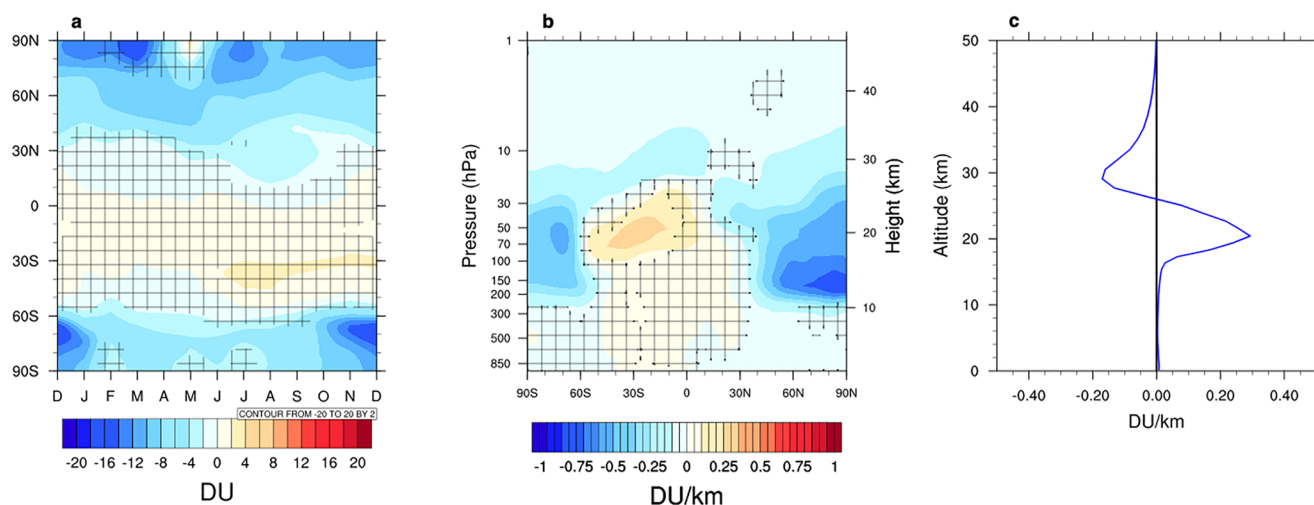


Figure 7. Similar to Figure 6 but instead the simulations compared are the 10 Gg/yr emission scenario with black carbon surface area density (BCSAD) removed from the overall sulfate surface area density (SulfSAD) and the control simulation (10 Gg/yr BCSAD—control case). The total column ozone anomaly (DU) is shown in panel (a). Column ozone anomaly has been converted into monthly averages and plotted against latitude. The annual zonal average ozone anomaly is shown in DU/km in panel (b). Statistically significant ozone anomalies are in areas where with no hatched lines (95% confidence interval). Panel (c) shows the annual average vertical profile of the ozone anomaly in DU/km from the surface to 50 km between 5° and 30°S.

The 30 and 100 Gg/yr emission scenarios produce a similar, but more extreme ozone response than seen in the 10 Gg/yr case. In both scenarios, the ozone response is statistically significant at almost all latitudes and altitudes (Figures S8 and S9 in Supporting Information S1).

Next, we investigate the mechanism of the ozone loss shown in Figure 6. At first glance, the NH high latitude pattern in Figures 6a and 6b looks consistent with the stratospheric ozone response to large volcanic eruptions which inject significant amounts of sulfate aerosol into the stratosphere. Sulfate aerosol emitted from large eruptions have been shown to invigorate ozone destroying heterogeneous chemistry due to an increase in surface area for reactions to occur on (i.e., Hofmann & Solomon, 1989; McCormick et al., 1995; Tie et al., 1994, Tie and Brasseur, 1995). Rocket emissions in our simulations are somewhat analogous to a large volcanic eruption as the emitted sulfate coated BC increases the sulfate surface area density (SulfSAD). Figure S10 in Supporting Information S1, which depicts the change in SulfSAD between the 10 Gg/yr case and the control simulation shows that there is an increase in SulfSAD with the introduction of BC emitted by rocket launches. However, the first panel in Figure S10 in Supporting Information S1, which shows the background stratospheric SulfSAD concentration in the control simulation, reveals that this increase in SulfSAD is still an order of magnitude less than the background concentration.

Furthermore, a simple test can be undertaken to see if the ozone response is indeed SulfSAD driven. An additional 10 Gg/yr emission simulation using an interactive ocean was performed that isolated the ozone response to temperature stimuli only. In this simulation, the BC surface area density (BCSAD) emitted into the stratosphere from rockets was removed so that the stratospheric SulfSAD became nearly equal to the control case SulfSAD. The ozone anomaly produced from the 10 Gg/yr minus BCSAD simulation can be seen in Figure 7. The temporal and spatial ozone anomaly in Figure 7 is quite similar to the ozone anomaly shown in Figure 6. The NH in Figure 7 experiences statistically significant ozone loss poleward of 30°N with an average magnitude and spatial pattern comparable to that of the normal 10 Gg/yr case. In this purely temperature driven simulation, more ozone loss occurs at the north pole in the fall and wintertime months. The ozone anomaly in the SH is statistically significant over most of the year poleward of 60°S with the greatest ozone loss occurring in the SH spring and summer (Figure 7a). The vertical extent of the ozone anomaly is nearly identical to the normal 10 Gg/yr emission scenario though more statistically significant ozone changes again occur poleward of 60°S (Figures 7b and 7c).

Changes in odd oxygen rates from key ozone destroying species are shown in Figure S11 in Supporting Information S1. Ozone can be chemically destroyed via various pathways with reactive nitrogen (NO_x), chlorine (ClO_x), bromine (BrO_x), and hydrogen radicals (HO_x) in the mid-to-lower stratosphere (<30 km). While Figure S11 in Supporting Information S1, shows that the fractional contribution to total odd oxygen loss for each reactant

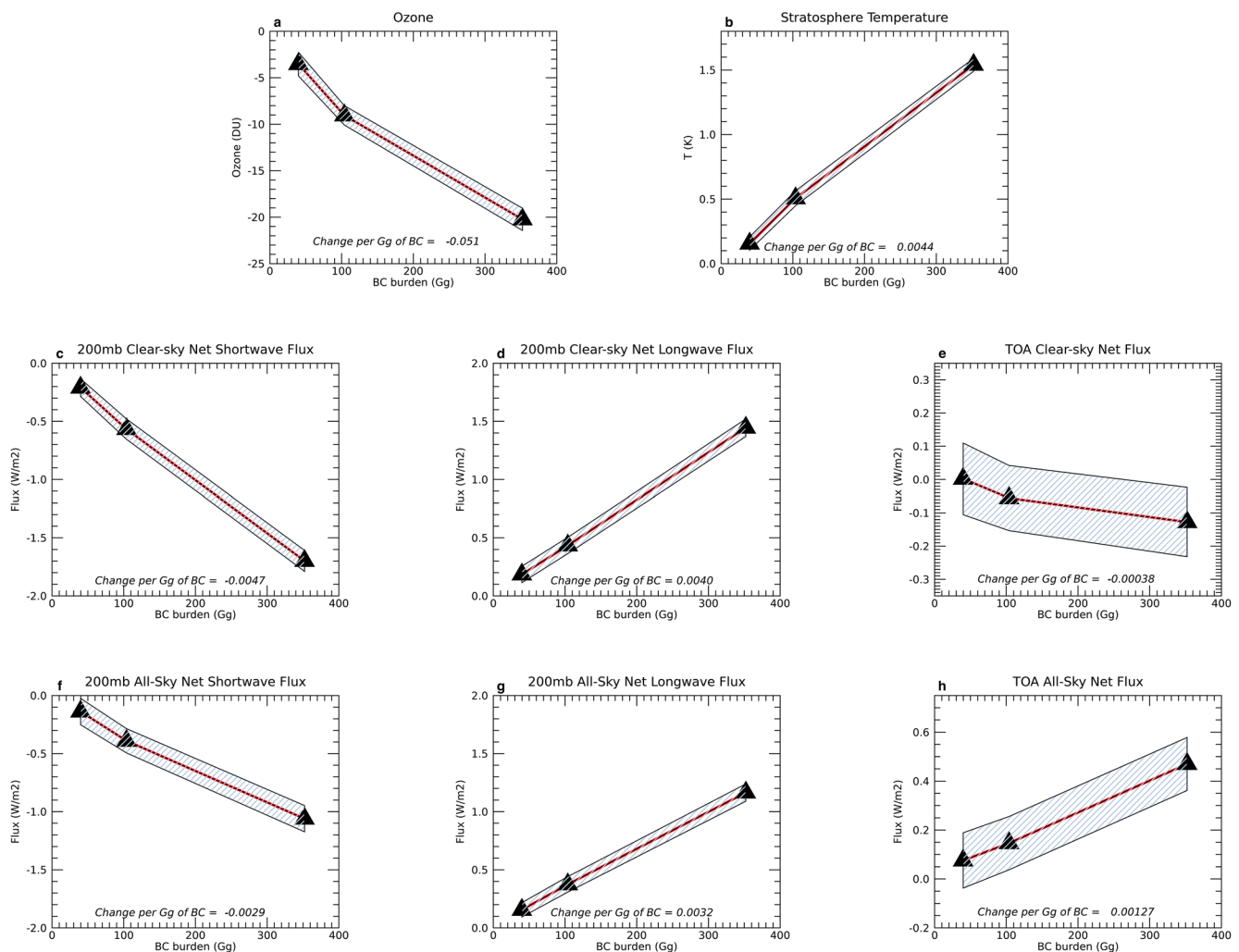


Figure 8. Annual stratospheric average temperature (panel a), ozone (panel b), 200 mb clear-sky net SWF (panel c), 200 mb clear-sky net LWF (panel d), the TOA clear-sky net flux (panel e), the 200 mb all-sky net SWF (panel f), the 200 mb all-sky net LWF (panel g), and the TOA all-sky net flux (panel g) trends due to increasing annual BC emissions (x -axis). The triangles represent the global annual average value. This value is also listed in Table 1 for each emission scenario. The shaded envelope shows the data 95% confidence interval. Results were produced by the interactive ocean simulation. The slope each respective line representing the change per gigagram of BC is listed at the bottom of each panel.

experience changes, these anomalies are small in scale. Furthermore, offsetting anomalies are prevalent in Figure S11 in Supporting Information S1. For example, the increase in odd oxygen loss due to HO_x chemistry between 10 and 30 km in the NH hemisphere is offset by a near equal negative anomaly in NO_x chemistry.

Taking Figures S10 and S11 in Supporting Information S1, and Figure 7 into consideration we find that the NH ozone response to rocket BC emissions shown in Figure 6 is primarily driven by warming the stratosphere and shifts in dynamics. The weaker NH overturning circulation exhibited in Figure 5 means that less ozone is transported from the tropics to high latitudes to replenish NH polar ozone concentrations (Figure 5).

3.5. Climate Response Scaling With Increased Emissions

Finally, we investigated two more extreme emission scenarios of 30 and 100 Gg/yr. Figure 8 shows how the climate response scales with increasing stratospheric BC emissions while Table 1 lists the global annual average values corresponding with the triangles in Figure 8. Surface temperature results shown here use the interactive ocean simulation while stratospheric temperature, ozone, and radiative forcing panels use the fixed SST simulation. The larger emission scenarios resulted in an annual average stratospheric burden of approximately 100 and

approximately 340 Gg for the 30 and 100 Gg/yr cases respectively (blue and green lines in Figure S1 in Supporting Information S1 and Table 1). We see from Figure 8 that the simulated climate response scales nearly linearly to increasing the annual stratospheric BC burden. For example, the global average stratospheric temperature anomaly shown in Figure 8b for the 10 Gg/yr case increases in a near linear fashion from approximately 0.15 to 0.5 K and 1.5 K for the 30 and 100 Gg/yr cases, respectively. The annual global average surface temperature anomaly also becomes larger with increasing emissions (Table 1). Both the 30 and 100 Gg simulations experience a statistically significant surface cooling of approximately -0.08 K and -0.2 K, respectively. For a frame of reference, the 2019 Australian wildfire event, which injected approximately 20 Gg of BC into the lower stratosphere produced a 0.06 K global cooling signal that lasted only a few months (Fasullo et al., 2021).

Next, ozone loss increases with increasing annual emissions (Figure 8a). The average annual global column ozone loss in the 10 Gg/yr case is approximately 3.4 DU and increases to over 20 DU in the 100 Gg/yr simulation (Table 1). Interestingly, the scaling between the 10 and 30 Gg/yr emission scenarios are more nonlinear than the scaling between the 30 and 100 Gg/yr emission scenarios. This result suggests that some threshold exists between the 10 and 30 Gg/yr BC burdens in which the climate response begins to scale more linearly. More research is required to ascertain whether this is a physical response or model bias. Though not shown here, it is important to note that in the 100 Gg/yr emission case, the simulated climate begins to resemble the climate shown in previous studies like Kravitz et al. (2012) which investigated a 1 Tg stratospheric BC injection.

Figure 8c shows the global annual average 200 mb clear-sky net shortwave flux change (SWF) at the tropopause level. Downwelling shortwave radiation for the 10 Gg case is reduced by approximately 0.21 W/m² due to stratospheric BC. This black carbon “umbrella” reduces downwelling shortwave radiation more strongly in the NH where more BC exists (Figure 3). Ross et al. (2010) estimated rocket BC would intercept about 0.3 W/m² per 10 Gg emission, similar to the model value calculated here. As with the other panels shown in Figure 8, the extreme emission scenarios result in a larger SWF response. Under 30 Gg/yr conditions, 0.56 W/m² is intercepted and as much as 1.7 W/m² is removed from the overall global 200 mb clear-sky SWF in the 100 Gg case. In comparison, the 2019 Australian Wildfire event induced a larger SWF of approximately -0.95 W/m², about five times larger than the SWF anomaly caused by the 10 Gg/yr emission scenario. However, the Australian fire event's SWF climate response lasted for a couple months before tapering off (Fasullo et al., 2021).

The 200 mb clear-sky net longwave flux change (LWF) in Figure 8d shows an inverse response to that of the SWF forcing. Downwelling LWF increases by approximately 0.18 W/m² in the 10 Gg case and is further strengthened by approximately 0.43 and 1.45 W/m² in the 30 and 100 Gg emission scenarios respectively. Comparing Figures 8c and 8d explains why such a strong reduction in downwelling SWF from rocket BC results in a relatively small TOA net flux (Figure 8e). When the stratosphere experiences a shortwave radiative forcing, such as warming caused by short wave absorbing BC aerosols, an adjustment will occur which results in a nearly equal opposing long wave forcing (Ban-Weiss et al., 2012). In the case exhibited here, the 200 mb SWF and LWF anomalies nearly cancel each other out and results in a small change in the TOA net flux in each emission scenario. Note that while we show the SWF and LWF changes at the tropopause a similar compensation occurs at the TOA.

Interestingly, the 10 Gg/yr case has a slightly positive TOA net flux of 0.002 W/m², while the 30 and 100 Gg/yr have negative TOA net fluxes of approximately -0.05 W/m² and approximately -0.127 W/m² respectively. However, both the 10 and 30 Gg/yr TOA net flux anomalies are smaller than annual variability within the default case (0.07 W/m², Table 1) and thus are not statistically significant.

Figures 8f, 8g, and 8h show the same radiative responses for the 200 mb SWF, 200 mb LWF, and TOA net flux but for all-sky. Both the SWF (Figure 8f) and LWF (Figure 8g) all-sky responses are relatively similar to the clear-sky. The most notable difference between the clear-sky and all-sky response in Figure 8 is that the TOA net flux (Figure 8h) reverses sign and experiences a statistically significant increase for the 30 and 100 Gg/yr emission scenarios (Table 1). The 10 Gg/yr simulation all-sky TOA net flux is quite small, but the 30 and 100 Gg/yr cases produce a significant climate response of 0.15 and 0.47 W/m², respectively. The radiation code in CESM directly calculates the all-sky and then diagnoses the clear-sky fluxes based upon the cloud fraction produced by the model. Therefore, it is possible that UT/LS ice clouds in the larger emission scenarios are being impacted by the portion of BC emissions which sediment out of the stratosphere (Figure 2, Figures S2 and S3 in Supporting Information S1), influencing the TOA radiation fluxes. An extensive investigation of the intricate cloud response

to these stratospheric BC emissions is beyond the scope of this study; however, future work to investigate the cloud response to rocket BC emissions is planned.

The results presented here compare well with the Kravitz et al. (2012) study which simulated a hypothetical geoengineering action plan of injecting 1 Tg/yr of BC into the stratosphere. The TOA net flux from their 1 Tg/yr injection ranged between -8.24 to -0.09 W/m² depending on the emission altitude and aerosol size distribution (Kravitz et al., 2012).

The results produced here are not dependent on the exact rocket source for BC. Figure 8 applies to rocket BC emissions in general and can be used to scale ozone loss for exhaust from different rocket propellant types. Figures 6 and 8 show global ozone loss of approximately 2.0% for a 10 Gg BC emission, corresponding to a liquid propellant (kerosene fuel) consumption of about 500 Gg. Similarly, chlorine gas emissions from solid rocket motor (SRM) exhaust have been shown to cause global ozone loss in a linearly scalable way (Jackman et al., 1998; Voigt et al., 2013) with about 0.02% global ozone loss for 7 Gg of solid propellant combustion into the stratosphere. Liquid and solid propellants therefore cause ozone loss of about 4% per Tg and 3% per Tg of propellant burned in the stratosphere, respectively. Thus, purely liquid propellant rockets, through BC emissions, cause about the same global ozone loss as purely solid propellant rockets. This work makes it clear that the aerosol emissions are important for estimating ozone loss from rockets and that chlorinated SRM rockets are not the only propellant type that should be included in assessments (WMO, 2018).

4. Conclusions

We performed a series of simulations using CESM2/WACCM6 to investigate how a projected increase in future spaceflight launches could impact Earth's atmosphere. This study is a continuation of earlier work performed by Ross et al. (2010) which focused on BC emissions from rockets. Here, we used an improved version of the state-of-the-art climate model with realistic background states and investigate larger annual emission scenarios. A range of emission scenarios were performed: 10, 30, and 100 Gg/yr. This study focused primarily on the 10 Gg/yr emission scenario which could occur within two decades if recent trends in launch rates continue and rockets continue to use engines with relatively large EI(BC).

We found that under a 10 Gg/yr emission scenario (with a launch site at 30 N) a BC “umbrella” accumulation forms which covers most of the stratosphere in both hemispheres with the largest concentrations of BC occurring within 20 degrees of the injection latitude in the NH. The stratospheric BC burden more than doubles. The stratospheric BC accumulation from simulated rocket launches has multiple effects across the stratosphere and troposphere including:

1. The increase in stratospheric BC leads to warming throughout the stratosphere by as much as 1.5 K in the annual mean. The strongest response occurs poleward of 30 N and is dominated by changes in JJA.
2. The interaction between seasonal solar heating and the asymmetrical BC distribution leads to an overall slowing of the Hadley cell and the global overturning circulation during DJF. Conversely, the overturning circulation becomes stronger during JJA due to a larger meridional temperature gradient.
3. Stratospheric ozone concentration decreases throughout the year at high latitudes in the NH. The greatest NH ozone column loss of approximately -16 DU occurs at the pole during boreal springtime. NH ozone is primarily driven by temperature increases altering stratospheric transport. The SH experiences fewer instances of statistically significant ozone loss, though the -6 DU anomaly at the south pole during the SH springtime suggests that a more severe Antarctic ozone hole may form in response to rocket BC emissions. SH ozone is driven by the combination of shifts in dynamics and odd oxygen destroying reaction rates.
4. The BC clear-sky TOA net flux for the 10 Gg/yr case is small relative to annual variability, but the 200 hPa SWF forcing is approximately 0.21 W/m², comparable to similar work produced by Ross et al. (2010). The small clear-sky TOA net flux is due to a large LWF forcing that counteracts much of the SWF forcing. However, the response in the all-sky TOA net flux suggests that UT/LS clouds may be impacted by the rocket emissions simulated here. While we note this important climate response, a detailed investigation of the cloud response is beyond the scope of the broad focus of this paper.
5. Over the range of BC emissions simulated, there is a near-linear relationship between the thermal, radiative, and ozone response and the amount of BC emitted into the stratosphere. Of these effects, the ozone and TOA

net flux responses show the largest degree of non-linearity which may be indicative of interacting processes at relatively small BC aerosol injection rates.

We conclude that if rocket engine technology remains unchanged and orbital launches become more frequent by a factor of 10, a significant stratospheric climate and ozone response is expected. Rocket BC emissions of this magnitude do not produce a simple stratospheric “umbrella” that cools the surface. Rather, complex radiative and dynamical changes produce patterns of warming and cooling. Previous models have examined the chemical role that space industry aerosols emissions play on stratospheric ozone. This work presents a first look at the radiative role spaceflight absorbing aerosols have on ozone. All spaceflight produced aerosols, including launch BC and alumina will need to be evaluated to produce a complete assessment of space industry emissions. Furthermore, submicron aerosol generated during re-entry “burn up” of defunct satellites will enter the stratosphere from the mesosphere and this source could increase substantially in the coming decade, possibly approaching the background meteoritic flux (Boley & Byers, 2021). This work provides directions for future research simulating the coupled climate and ozone response to these aerosols. This study gives an estimate on the impacts due to the dirtiest rocket types, but the stratospheric particulate population will be increasingly affected by human activities and all sources of these particles need to be better understood. To fully assess the space flight impact on climate, comprehensive inventories and scenarios of spaceflight emissions are needed.

Data Availability Statement

The model output from our CESM2/WACCM6 simulations used in the analysis of this study is open to the public. The data can be found at NOAA's Chemistry and Climate Processes Supporting Data webpage (https://csl.noaa.gov/groups/csl8/modeldata/data/Maloney_et_al_2021/ [Maloney et al., 2022]).

Acknowledgments

The work performed here by Dr. C. Maloney was supported by NOAA's Earth's Radiation Budget initiative, NOAA CPO Climate & CI #03-01-07-001. High performance computing was performed with the Hera computer supported by NOAA. The authors would like to thank Dr. M. Mills of NCAR for his assistance in the porting of the CESM2 model used in this study onto the Hera supercomputer. The authors would also like to thank Dr. D. W. Fahey, Dr. M. Mills, and Dr. S. Tilmes for helpful discussions.

References

- Ailor, W. (2021). Hazards of reentry disposal of satellites from large constellations. *Journal of Space Safety Engineering*, 6, 2. <https://doi.org/10.1016/j.jsse.2019.06.005>
- Ban-Weiss, G., Cao, L., Bala, G., & Caldeira, K. (2012). Dependence of climate forcing and response on the altitude of black carbon aerosols. *Climate Dynamics*, 38, 897–911. <https://doi.org/10.1007/s00382-011-1052-y>
- Blake, D. F., & Kato, K. (1995). Latitudinal distribution of black carbon soot in the upper troposphere and lower stratosphere. *Journal of Geophysical Research*, 100(D4), 7195–7202. <https://doi.org/10.1029/94JD03118>
- Boley, A. C., & Byers, M. (2021). Satellite mega-constellations create risks in Low Earth Orbit, the atmosphere and on Earth. *Scientific Reports*, 11, 10642. <https://doi.org/10.1038/s41598-021-89909-7>
- Butchart, N. (2014). The Brewer-Dobson circulation. *Reviews of Geophysics*, 52, 157–184. <https://doi.org/10.1002/2013RG000448>
- Danabasoglu, G., Lamarque, J.-F., Bacmeister, J., Bailey, D. A., DuVivier, A. K., Edwards, J., et al. (2020). The community Earth system model version 2 (CESM2). *Journal of Advances in Modeling Earth Systems*, 12, e2019MS001916. <https://doi.org/10.1029/2019MS001916>
- De Luca, L., Galfetti, L., Maggi, F., Colombo, G., Merotto, L., Boiocchi, M., et al. (2013). Characterization of HTPB-based solid fuel formulations: Performance, mechanical properties, and pollution. *Acta Astronautica*, 92, <https://doi.org/10.1016/j.actaastro.2012.05.002>
- Fasullo, J. T., Rosenbloom, N., Buchholz, R. R., Danabasoglu, G., Lawrence, D. M., & Lamarque, J.-F. (2021). Coupled climate responses to recent Australian wildfire and COVID-19 emissions anomalies estimated in CESM2. *Geophysical Research Letters*, 48, e2021GL093841. <https://doi.org/10.1029/2021GL093841>
- Gettelman, A., Mills, M. J., Kinnison, D. E., Garcia, R. R., Smith, A. K., Marsh, D. R., et al. (2019). The whole atmosphere community climate model version 6 (WACCM6). *Journal of Geophysical Research: Atmospheres*, 124, 12380–12403. <https://doi.org/10.1029/2019jd030943>
- Grewe, V., Stenke, A., Ponater, M., Sausen, R., Pitari, G., Iachetti, D., et al. (2007). Climate impact of supersonic air traffic: An approach to optimize a potential future supersonic fleet – results from the EU-project SCENIC. *Atmospheric Chemistry and Physics*, 7, 5129–5145. <https://doi.org/10.5194/acp-7-5129-2007>
- Hofmann, D. J., & Solomon, S. (1989). Ozone destruction through heterogeneous chemistry following the eruption of El Chichón. *Journal of Geophysical Research*, 94(D4), 5029–5041. <https://doi.org/10.1029/JD094iD04p05029>
- Jackman, C. H., Conside, D. B., & Fleming, E. L. (1998). A global modeling study of solid rocket aluminum oxide emission effects on stratospheric ozone. *Geophysical Research Letters*, 25, 907–910. <https://doi.org/10.1029/98GL00403>
- Jones, H. (2018). *The recent large reduction in space launch cost*. 48th International Conference on Environmental Systems ICES-2018-81.
- Kinnison, D., Brasseur, G. P., Baughcum, S. L., Zhang, J., & Wuebbles, D. (2020). The impact on the ozone layer of a potential fleet of civil hypersonic aircraft. *Earth's Future*, 8, e2020EF001626. <https://doi.org/10.1029/2020ef001626>
- Kravitz, B., Robock, A., Shindell, D. T., & Miller, M. A. (2012). Sensitivity of stratospheric geoengineering with black carbon to aerosol size and altitude of injection. *Journal of Geophysical Research*, 117, D09203. <https://doi.org/10.1029/2011JD017341>
- Larson, E. J. L., Portmann, R. W., Rosenlof, K. H., Fahey, D. W., Daniel, J. S., & Ross, M. N. (2017). Global atmospheric response to emissions from a proposed reusable space launch system. *Earth's Future*, 5, 37–48. <https://doi.org/10.1002/2016EF000399>
- Lee, D. S., Fahey, D. W., Skowron, A., Allen, M. R., Burkhardt, U., Chen, Q., et al. (2021). The Contribution of Global Aviation to Anthropogenic Climate Forcing for 2000 to 2018. *Atmospheric Environment*, 244, 1352–2310. <https://doi.org/10.1016/j.atmosenv.2020.117834>
- Lee, D. S., Pitari, G., Grewe, V., Gierens, K., Penner, J. E., Petzold, A., et al. (2010). The impacts on atmosphere and climate: Aviation. *Atmospheric Environment*, 44(37), 1352–2310. <https://doi.org/10.1016/j.atmosenv.2009.06.005>

- Li, F., Waugh, D. W., Douglass, A. R., Newman, P. A., Strahan, S. E., Ma, J., et al. (2012). Long-term changes in stratospheric age spectra in the 21st century in the Goddard Earth observing system chemistry-climate model (GEOSCCM). *Journal of Geophysical Research*, *117*, D20119. <https://doi.org/10.1029/2012JD017905>
- Linz, M., Plumb, R., Gerber, E., Haenel, F. J., Stiller, G., Kinnison, D. E., et al. (2017). The strength of the meridional overturning circulation of the stratosphere. *Nature Geoscience*, *10*, 663–667. <https://doi.org/10.1038/ngeo3013>
- Liu, X., Ma, P.-L., Wang, H., Tilmes, S., Singh, B., Easter, R. C., et al. (2016). Description and evaluation of a new four-mode version of the modal aerosol module (MAM4) within version 5.3 of the community atmosphere model. *Geoscientific Model Development*, *9*, 505–522. <https://doi.org/10.5194/gmd-9-505-2016>
- Maloney, C. M., Portmann, R. W., Ross, M. N., & Rosenlof, K. H. (2022). The climate and ozone impacts of black carbon emissions from global rocket launches – model simulation output [Data Set]. NOAA Chemical Sciences Laboratory: Chemistry & Climate Processes Group's Supporting Data Repository. Retrieved from https://csf.noaa.gov/groups/csl8/modeldata/data/Maloney_etal_2021/
- Marsh, D. R., Mills, M. J., Kinnison, D. E., Lamarque, J., Calvo, N., & Polvani, L. M. (2013). Climate change from 1850 to 2005 simulated in CESM1 (WACCM). *Journal of Climate*, *26*(19), 7372–7391. <https://doi.org/10.1175/jcli-d-12-00558.1> Retrieved from <https://journals.amet-soc.org/view/journals/clim/26/19/jcli-d-12-00558.1.xml>
- Matthes, S., Lee, D. S., De Leon, R. R., Lim, L., Owen, B., Skowron, A., et al. (2022). Review: The effects of supersonic aviation on ozone and climate. *Aerospace*, *9*, 41. <https://doi.org/10.3390/aerospace9010041>
- McCormick, M., Thomason, L., & Trepte, C. (1995). Atmospheric effects of the Mt Pinatubo eruption. *Nature*, *373*, 399–404. <https://doi.org/10.1038/373399a0>
- Mills, M., Toon, O., Turco, R., Kinnison, D., & Garcia, R. (2008). Massive global ozone loss predicted following nuclear conflict. *Proceedings of the National Academy of Sciences of the United States of America*, *105*, 5307–5312. <https://doi.org/10.1073/pnas.0710058105>
- Murtaza, A., Pirzada, S. J. H., Xu, T., & Jianwei, L. (2020). Debris threat for space sustainability and way forward. *IEEE Access*, *8*, 61000–61019. <https://doi.org/10.1109/ACCESS.2020.2979505>
- Newman, P., Wilson, J. C., Ross, M. N., Brock, C. A., Sheridan, P. J., Schoeberl, M. R., et al. (2001). Chance encounter with a stratospheric kerosene rocket plume from Russia over California. *Geophysical Research Letters*, *28*, 959–964. <https://doi.org/10.1029/2000GL011972>
- Penner, J. E., Lister, D. H., Griggs, D. J., Dokken, D. J., & McFarland, M. (Eds.) (1999). *Aviation and the global atmosphere* (pp. 1–373). Cambridge University Press.
- Ross, M., Mills, M., & Toohey, D. (2010). Potential climate impact of black carbon emitted by rockets. *Geophysical Research Letters*, *37*, L24810. <https://doi.org/10.1029/2010GL044548>
- Ross, M., & Toohey, D. (2019). *The coming surge of rocket emissions*. EOS.
- Ross, M., Toohey, D. W., Rawlins, W. T., Richard, E. C., Kelly, K. K., Tuck, A. F., et al. (2000). Observation of stratospheric ozone depletion associated with Delta II rocket emissions. *Geophysical Research Letters*, *27*, 2209–2212. <https://doi.org/10.1029/1999GL011159>
- Ross, M., & Vedda, J. (2018). *The policy and science of rocket emissions*. The Aerospace Corporation. Retrieved from https://aerospace.org/sites/default/files/2018-05/RocketEmissions_0.pdf
- Simmons, F. (2001). *Rocket exhaust plume phenomenology*. The Aerospace Press.
- Stettler, M., Boies, A. M., Petzold, A., & Barrett, S. R. H. (2013). Global civil aviation black carbon emissions. *Environmental Science and Technology*, *130823150610008*. <https://doi.org/10.1021/es401356v>
- Strykowski, J. (2001). *Soot mass loading and particle size effects on laser backscatter from rocket plumes* (pp. 2001–356). AIAA.
- Tie, X., & Brasseur, G. (1995). The response of stratospheric ozone to volcanic eruptions: Sensitivity to atmospheric chlorine loading. *Geophysical Research Letters*, *22*, 3035–3038. <https://doi.org/10.1029/95gl03057>
- Tie, X. X., Brasseur, G. P., Briegleb, B., & Granier, C. (1994). Two-dimensional simulation of Pinatubo aerosol and its effect on stratospheric ozone. *Journal of Geophysical Research*, *99*, 20545–20562. <https://doi.org/10.1029/94JD01488>
- Toon, O. B., Turco, R. P., Westphal, D., Malone, R., & Liu, M. S. (1988). A multidimensional model for aerosols: Description of computational analogs. *Journal of the Atmospheric Sciences*, *45*(15), 2123–2143. [https://doi.org/10.1175/1520-0469\(1988\)045<2123:ammfad>2.0.co;2](https://doi.org/10.1175/1520-0469(1988)045<2123:ammfad>2.0.co;2)
- Turco, R. P., Toon, O. B., Pollack, J. B., Whitten, R. C., Poppoff, I. G., & Hamill, P. (1980). Stratospheric aerosol modification by supersonic transport and space shuttle operations—climate implications. *Journal of Applied Meteorology and Climatology*, *19*(1), 78–89. [https://doi.org/10.1175/1520-0450\(1980\)019<0078:sambst>2.0.co;2](https://doi.org/10.1175/1520-0450(1980)019<0078:sambst>2.0.co;2)
- Visioni, D., Tilmes, S., Bardeen, C., Mills, M., MacMartin, D. G., Kravitz, B., & Richter, J. H. (2022). Limitations of assuming internal mixing between different aerosol species: A case study with sulfate geoengineering simulations. *Atmospheric Chemistry and Physics*, *22*, 1739–1756. <https://doi.org/10.5194/acp-22-1739-2022>
- Voigt, C., Schumann, U., Graf, K., & Gottschaldt, K.-D. (2013). Impact of rocket exhaust plumes on atmospheric composition and climate – An overview. In: *European Conference for Aerospace Sciences*, (pp. 3–16). <https://doi.org/10.1051/eucass/201304657>
- Wang, Y., Ma, P.-L., Peng, J., Zhang, R., Jiang, J. H., Easter, R. C., & Yung, Y. L. (2018). Constraining aging processes of black carbon in the Community Atmosphere Model using environmental chamber measurements. *Journal of Advances in Modeling Earth Systems*, *10*, 2514–2526. <https://doi.org/10.1029/2018ms001387>
- Waugh, D. W., & Hall, T. M. (2002). Age of stratospheric air: Theory, observations, and models. *Reviews of Geophysics*, *40*(4), 1010. <https://doi.org/10.1029/2000RG000101>
- Weisenstein, D. K., Keith, D. W., & Dykema, J. A. (2015). Solar geoengineering using solid aerosol in the stratosphere. *Atmospheric Chemistry and Physics*, *15*, 11835–11859. <https://doi.org/10.5194/acp-15-11835-2015>
- World Meteorological Organization. (2018). *Scientific assessment of ozone depletion: 2018*. Global Ozone Research and Monitoring Project – report No. 58, 588.
- Yu, P., Davis, S. M., Toon, O. B., Portmann, R. W., Bardeen, C. G., Barnes, J. E., et al. (2021). Persistent stratospheric warming due to 2019–2020 Australian wildfire smoke. *Geophysical Research Letters*, *48*, e2021GL092609. <https://doi.org/10.1029/2021GL092609>
- Yu, P., Toon, O. B., Bardeen, C. G., Zhu, Y., Rosenlof, K. H., Portmann, R. W., et al. (2019). Black carbon lofts wildfire smoke high into the stratosphere to form a persistent plume. *Science*, *365*, 587–590. <https://doi.org/10.1126/science.aax1748>
- Zhang, J., Wuebbles, D., Kinnison, D., & Baughcum, S. L. (2021a). Potential impacts of supersonic aircraft emissions on ozone and resulting forcing on climate: An update on historical analysis. *Journal of Geophysical Research: Atmospheres*, *126*, e2020JD034130. <https://doi.org/10.1029/2020JD034130>
- Zhang, J., Wuebbles, D., Kinnison, D., & Baughcum, S. L. (2021b). Stratospheric ozone and climate forcing sensitivity to cruise altitudes for fleets of potential supersonic transport aircraft. *Journal of Geophysical Research: Atmospheres*, *126*, e2021JD034971. <https://doi.org/10.1029/2021JD034971>

References From the Supporting Information

- Alexeenko, A., Gimelshein, N. E., Levin, D. A., Collins, R. J., Rao, R., Candler, G. V., et al. (2002). Modeling of flow and radiation in the atlas plume. *Journal of Thermophysics and Heat Transfer*, *16*(1). <https://doi.org/10.2514/2.6651>
- Burt, J., & Boyd, I. (2007). High-altitude plume simulations for a solid propellant rocket. *AIAA Journal*, *1013*, 10.2514/1.30129. <https://doi.org/10.2514/6.2007-1013>
- Chang, V., & Chern, R. (2021). A preliminary study on the potential spaceports for suborbital space tourism and intercontinental point-to-point transportation in Taiwan. *Acta Astronautica*, *181*, 492–502. <https://doi.org/10.1016/j.actaastro.2020.11.059>
- Farmer, R., Smith, S. D., & Myruski, B. L. (1994). *Radiation from advanced solid rocket motor plumes*. SECA Inc. Contract No. NAS8-393.
- Plastinin, Y., Karabdzhak, G., Khmelinin, B., Baula, G., & Rodionov, A. (2001). *Ultraviolet, visible, and infrared spectra modeling for solid and liquid-fuel rocket exhausts*. AIAA. <https://doi.org/10.2514/6.2001-660>
- Snelling, D., Thomson, K. A., Smallwood, G. J., Gulder, O. L., Weckman, E. J., & Fraser, R. A. (2002). Spectrally resolved measurement of flame radiation to determine soot temperature and concentration. *AIAA Journal*, *40*, 1789–1799. <https://doi.org/10.2514/3.15261>
- Wright, M., Rao, R., Candler, G., Hong, J., Schilling, T., & Levin, D. (1998). Modeling issues in the computation of plume radiation signatures. *AIAA*, 98–3622. <https://doi.org/10.2514/6.1998-3622>
- Zhang, X., Chen, X., & Wang, J. (2019). A number-based inventory of size-resolved black carbon particle emissions by global civil aviation. *Nature Communications*, *10*, 534. <https://doi.org/10.1038/s41467-019-08491-9>